PNAS RESEARCH ARTICLE | APPLIED MATHEMATICS OPEN ACCESS

Quantifying the hierarchical topological decay of fluid knots

Xin Liu[a,1], Renzo L. Ricca[a,b,c,2], and Yongrong Zhuo[a,d,1]

Edited by H. K. Moffatt, University of Cambridge, Cambridge, United Kingdom; received February 25, 2026; accepted August 15, 2026

In this paper we analyze the hierarchical topological cascade of knotted and linked filaments associated with the natural decay of superfluid vortex tangles. This is done by using an algebraic reformulation of knot polynomial invariants to quantify the topological states of the cascade process. By interpreting the evolutionary paths associated with vortex knot dynamics as geodesic flows in an appropriate knot polynomial space defined by adapted Jones polynomials [X. Liu, R. L. Ricca, *J. Phys. A Math. Theor.* 45, 205501 (2012).], we introduce an entanglement index to quantify the probability density of occurrence of each topological state. By this method we analyze all prime knots, links, and composites up to 8 crossings, and show that this measure detects accurately the decreasing topological complexity observed in simulations and laboratory experiments. By a comparative analysis carried out with data based on an alternative measure (complexity degree), we show that this entanglement index proves to be a more robust and reliable quantifier. The theoretical framework proposed here can be applied to other types of physical systems, where networks of filamentary structures are subject to continuous topological change and reorganization.

topological fluid mechanics | Jones knot polynomial | vortex knots | vortex links | superfluid tangle

Significance

Knotted and linked filamentary structures forming complex tangles are present in a wide variety of physical and biological systems. In the case of superfluid flows these tangles are made by a complex network of vortex filaments that are subject to continuous interaction and recombination. As a result, their vortex topology progressively simplifies producing elementary loops. Here, by exploiting an algebraic formulation of the knot polynomial invariants that characterize the tangle topology, we show that the measured probability of occurrence of the different topological states that emerge during evolution quantifies the observed topological cascade consistently with computed data and experimental observations. The method proposed in this work is applicable to other physical systems that exhibit similar features.

In this paper we analyze the probability density of occurrence of different topological states that appear in the evolutionary decay of superfluid vortex tangles, where knots and links are formed, interact, and reconnect by changing topology and crossing number during evolution. This is done by introducing an entanglement index to detect and quantify the topological states of vortex knots, links, and composites (up to 8 crossings) observed in experiments, which proves to be a robust and reliable detector of the topological cascade produced by vortex knot dynamics.

The present work follows the same philosophy carried out by Stolz et al. (1) on the topological simplification paths realized by recombinant DNA plasmids. In that case the study focused on the effects of the local action of certain enzymes (such as type II topoisomerase) on the DNA molecule that triggers a double-strand break, an exchange, and a rejoining of the free ends. Under the assumption of a stepwise reduction of crossing number the recursive application of DNA recombination leads to a gradual simplification of topological complexity. By using a combination of theoretical results and Monte Carlo simulations the authors established a probability pattern of simplification pathways identifying the most probable paths.

The same qualitative process takes place in other physical contexts, such as vortex dynamics, where site-specific enzyme actions are replaced by viscosity-driven reconnections, or other specific mechanisms, that produce similar effects. By applying appropriately defined knot polynomials to a family of torus knots and links Liu and Ricca (2) detected the optimal simplification pathway found by Stolz et al. and then, by introducing a different approach based on the use of adapted Jones polynomials applied to the same set of knots, they were able to reproduce accurately the same probability distribution (3). Given the success of this alternative method we propose to follow the same strategy employing a wider class of knot polynomials, by extending the analysis to a richer set of knots, links, and composites.

Complex networks of localized filamentary structures forming knots and links appear in a wide variety of physical and biological contexts, from fluid mechanics, plasma physics, geometric optics, to polymer physics, soft and biological matter, DNA biology (4–8), just to mention a few. Thin vortex filaments and defects represent a common feature in classical and quantum turbulence, and their detailed geometric and topological identification proves useful to quantify contents and transfers of energy across scales (9–11). These structures tend to form complex knots and links in space that due to their mutual interactions, reconnections, and natural fragmentation tend to decay during evolution. The typical process is governed by the gradual simplification of the initial topology with the formation of increasingly simpler structures leading up to the final creation of unknotted, unlinked loops (Fig. 1) (12–16). This hierarchical

Author affiliations: [a]Institute of Theoretical Physics, School of Physics and Optoelectronic Engineering, Beijing University of Technology, Beijing 100124, China; [b]Department of Mathematics and Applications, University of Milano-Bicocca, Milano 20125, Italy; [c]World Premier Institute for Sustainability with Knotted Chiral Meta Matter, Hiroshima University, Hiroshima 739-8526, Japan; and [d]Center for Theoretical Physics, College of Physics, Jilin University, Changchun 130012, China

Author contributions: X.L. and R.L.R. designed research; X.L. and R.L.R. performed research; X.L. and R.L.R. analyzed data; Y.Z. did the computation; and R.L.R. wrote the paper.

The authors declare no competing interest.

This article is a PNAS Direct Submission.

Copyright © 2026 the Author(s). Published by PNAS. This open access article is distributed under Creative Commons Attribution License 4.0 (CC BY).

[1]X.L. and Y.Z. contributed equally to this work.

[2]To whom correspondence may be addressed. Email: renzo.ricca@unimib.it.

This article contains supporting information online at https://www.pnas.org/lookup/suppl/doi:10.1073/pnas.2606419123/-/DCSupplemental.

Published November 12, 2026.

Downloaded from https://www.pnas.org by 95.75.213.112 on November 12, 2026 from IP address 95.75.213.112.

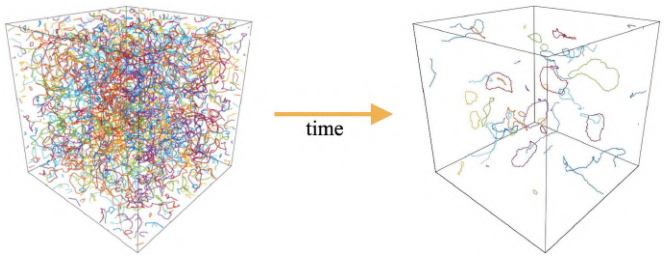

Fig. 1. Initial and final stages of the numerical time evolution of a complex tangle of quantum vortex filaments governed by the Gross–Pitaevskii equation. The snapshots taken at simulation time (*Left*) $t = 12$ and (*Right*) $t = 105$ show the disintegration of the vortex tangle with the final production of isolated unknotted, unlinked loops (adapted from ref. 9).

cascade from topologically complex vortex tangles to simpler, small scale structures is characterized by a time sequence of a step-wise unlinking process that occurs locally on vortex strands.

An elementary example is the topological decay of a trefoil vortex knot ($\boldsymbol{T}$) in water as observed in laboratory experiments (12). Once produced, the 3-crossing knot reconnects to form a Hopf link ($\boldsymbol{H}$) made by two interlaced vortex loops that recombine further to form a single, convoluted unknot ($\boldsymbol{U}$) (no topological crossings); after further reconnection a pair of unlinked, unknotted loops is formed. More complex examples have been observed and analyzed in superfluid simulations (16–18), where defects in the shape of torus knots with 9 crossings and Borromean rings ($\boldsymbol{B}$) with 6 crossings are observed to gradually simplify in time, going through various intermediate states of lower topological complexity (Fig. 2, *Left*). This simplification process has been observed not only in classical and quantum fluids (19), but also in magnetic fields (5, 20), optics (21), soft and biological matter, (7), liquid crystals (22), defects in condensed matter (23), and even in recombinant DNA plasmids (1).

The work of Cooper et al. (24, 25) for instance has shown the existence of a wide spectrum of knot topologies in superfluid tangles. By taking the highest degree ν of the Alexander knot polynomial (26) as an approximate measure of knot complexity, Barenghi and collaborators detected monster knots of extremely complex topology, with $\nu = \mathcal{O}(100)$. The particular decaying process and its physical details are not unique, and depend crucially on the initial conditions, but some qualitative features have a generic character. If several strands of a highly convoluted knot happen to interact simultaneously, multiple reconnections can take place at different locations inducing a dramatic change of the knot topology (i.e. a "topological collapse") by an instantaneous reduction of complexity (16). In other cases the interaction with nearby knots may even result in an increase of topological complexity ("reverse cascade") by generating transitional, short-lived loops with higher crossings (Fig. 2, *Right*).

Methods to determine preferential decaying paths are necessary to understand dynamical features and associated energy transfers across scales. A call in this direction needs a combined use of techniques borrowed from physical knot theory and fluid mechanics (8). Here we endeavor to carry out this approach. In the light of our previous work (3) we consider fluid knots, links, and composites up to 8 crossings, where each knot/link is represented by an oriented loop, whose orientation is induced by vorticity. This means also that any topological change due to vortex reconnection is an orientation preserving event on the reconnected strands; each topological state is then identified by the Jones polynomial invariant (26). This polynomial distinguishes all oriented prime knots up to 8 crossings, but it fails to separate certain oriented links and composite knot isotopy classes. As other knot polynomials, it is a strong topological detector, but is still an imperfect knot/link classifier.

The evolutionary unlinking paths are interpreted as geodesic flows in an abstract knot polynomial space. The physical occurrence of a topological state is computed through the metric properties of this space, and the most probable decaying paths are thus determined by estimating their probability density of occurrence. Alternative methods based on the analysis of shortest paths in weighted graphs have been developed and used in many disparate contexts (27–29), but the method proposed here relies explicitly on the exploitation of the topological features of the physical knot types observed in the process.

Methods

In a previous paper (3) we introduced the concept of knot polynomial space to describe and quantify the topological dynamics of fluid knots in terms of geodesic paths. This was done by using the adapted version of standard knot polynomials, such as Jones and HOMFLYPT (30, 31). Remember that the standard version of a knot polynomial is an invariant of an oriented knot/link $\mathcal{K}$, which assigns to each oriented $\mathcal{K}$ a Laurent polynomial in a dummy variable with integer coefficients; the adapted version (32) relates the dummy variable to the writhe and twist helicity contributions of the vortex knot/link. Previous work was limited to the analysis of knot types up to 6 crossings using the adapted Jones polynomial $V_{\mathcal{K}}(q)$ restricted to the algebraic expression given by purely positive signs of the exponents. Now we consider all knots, links, and composites up to 8 crossings using the same Jones polynomial, but with no restriction on the algebraic sign of their exponents. This entails an approach for the computation of the metric basis of the polynomial space. Let us introduce the following:

Definition 1 **(Knot polynomial space):** The knot polynomial space $\mathcal{V}_n$ is an n-dimensional, discrete, Euclidean space endowed by Euclidean metric (to be defined below), whose single points (singletons) are the adapted Jones polynomials of each knot type.

Since each singleton represents a specific physical knot or link $\mathcal{K}$ identified by its Jones polynomial $V_{\mathcal{K}}(q)$, it makes sense to choose the unknot $\boldsymbol{U}$ (whose polynomial value $V_{\boldsymbol{U}} = 1$) as the origin of the metric space $\mathcal{V}_n$. Since topological complexity is graded by the topological crossing number $c_{\min}$ of the knot type $\mathcal{K}$, the knot space is discretized by the iso-$c_{\min}$ level sets given by the discrete family of singletons determined by the Jones polynomial. The dynamical flows associated with the time evolution of the vortex knots are thus represented by the unlinking paths that connect different topological states (represented by the long arrows in the diagram of Fig. 2, *Right*) given by piece-wise linear geodesics on $\mathcal{V}_n$.

Downloaded from https://www.pnas.org by 95.75.213.112 on November 12, 2026 from IP address 95.75.213.112.

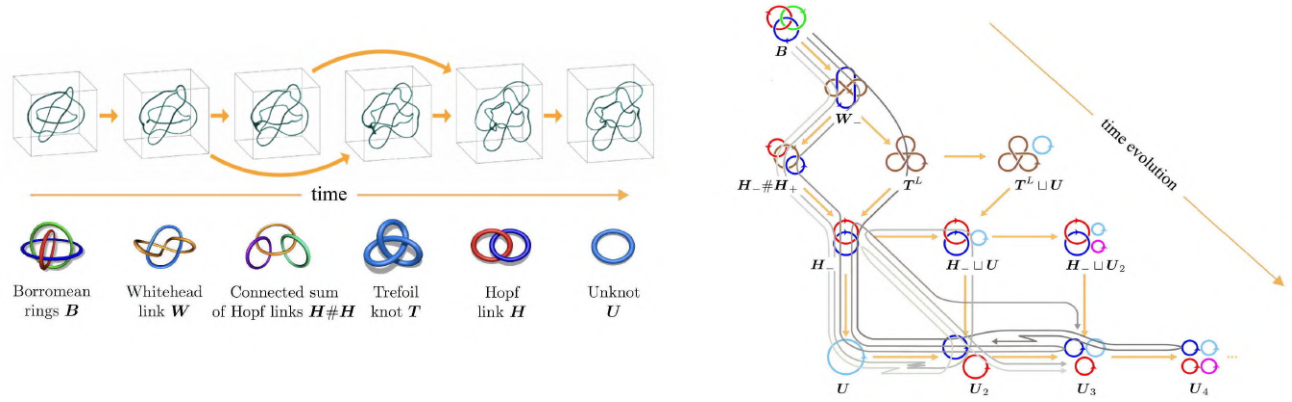

Fig. 2. (*Left*) Snapshots of the time evolution of quantum Borromean vortex rings governed by the Gross–Pitaevskii equation and schematic illustration of the corresponding topological states produced by step-wise reconnections. (*Right*) Diagram of the decaying paths associated with the evolutionary cascade of quantum Borromean vortex rings (***B***) observed in numerical simulations (18). The initial configuration decays forming a negative Whitehead link $\boldsymbol{W}_-$, and then a connected sum of negative and positive Hopf link $\boldsymbol{H}_-\#\boldsymbol{H}_+$, and/or a left-handed trefoil knot $\boldsymbol{T}^L$, followed by the formation of an isolated negative Hopf link $\boldsymbol{H}_-$, and disjoint unions with single or multiple unknots ($\boldsymbol{U}_1$, $\boldsymbol{U}_2$, etc.). Instances of inverse cascade (denoted by the zigzag long arrows) take place during the final stages of the process. Long arrows denote topological transitions, and arrows on the knot pictograms denote the vorticity orientation. Courtesy of Hao Guan, adapted from ref. 18.

Metric Basis of the Knot Polynomial Space and Knot Coordinates. To compute the geodesic flows that represent the decaying paths of vortex dynamics we must determine the position and the relative distance of the singletons given by the knot types. For this we must introduce an appropriate metric (hence a basis) on $\mathcal{V}_n$. Since each singleton is expressed through the Jones polynomial, whose algebraic expression includes positive and negative powers, we proceed with an algebraic reformulation of the polynomial that helps to elaborate independently terms containing only positive powers and terms containing only negative powers. This is done by rewriting the standard polynomial $V_{\mathcal{K}}$ in an algebraic complex form $\bar{V}_{\mathcal{K}}$, so that the real part of $\bar{V}_{\mathcal{K}}$ contains only positive powers, and the imaginary part only negative powers. From $\bar{V}_{\mathcal{K}}$ we derive then the complex expansion form $\widetilde{V}_{\mathcal{K}}$ that will be used to compute the metric coefficients.

For the first step it is convenient to take $q = x^2$ and express $V_{\mathcal{K}}(q)$ in terms of the new (dummy) variable x: recalling that the Jones polynomial is a Laurent polynomial in the (new) variable x, we have

$$V_{\mathcal{K}}(x) = \sum_{r=-m}^{n} a_r x^r = \sum_{j=1}^{m} a_{-j} x^{-j} + \sum_{i=0}^{n} a_i x^i, \qquad [1]$$

where the coefficient $a_r \in \mathbb{Z}$, taking (in general) $m \neq n$ (m, n integers). This formal rewrite helps to collect terms containing all purely *negative* powers, and terms containing all purely *nonnegative* powers into two groups given by the two summands on the right-hand side of Eq. **1**. Let us consider the first summand: by changing $x^{-1} \mapsto x$ and applying the "Wick's rotation" $\mathbb{R} \to \mathrm{i}\mathbb{R}$ ($\mathrm{i} = \sqrt{-1}$) to these terms, we can group them into the imaginary part of an algebraic complex form of $V_{\mathcal{K}}(x)$, so that

$$V_{\mathcal{K}}(x) \;\mapsto\; \bar{V}_{\mathcal{K}}(x) = \mathrm{i} \sum_{j=1}^{m} a_{-j} x^j + \sum_{i=0}^{n} a_i x^i . \qquad [2]$$

For practical reasons it is convenient to extract a_0 from the second summand and write

$$\bar{V}_{\mathcal{K}}(x) = \mathrm{i} \sum_{j=1}^{m} a_{-j} x^j + a_0 + \sum_{i=1}^{n} a_i x^i . \qquad [3]$$

$\bar{V}_{\mathcal{K}}(x)$ involves now only purely positive powers, that will be more easily managed for the computation of the metric coefficients. Moreover, since the Jones polynomial of a knot and its mirror counterpart are both defined by the same algebraic structure with opposite exponent signs, the proposed decomposition has the additional advantage of capturing mirror knots.

For the sake of example let us see how this transformation acts on the Jones polynomial of the left-handed trefoil knot $\boldsymbol{T}^L$:

$$V_{\boldsymbol{T}^L}(x) = -x^{-8} + x^{-6} + x^{-2} \qquad \longmapsto \qquad \bar{V}_{\boldsymbol{T}^L}(x) = \mathrm{i}\big(-x^8 + x^6 + x^2\big); \qquad [4]$$

and similarly for the Whitehead link $\boldsymbol{W}$, that involves positive and negative powers:

$$V_{\boldsymbol{W}}(x) = x^{-7} - 2x^{-5} + x^{-3} - 2x^{-1} + x - x^3 \qquad \longmapsto \qquad \bar{V}_{\boldsymbol{W}}(x) = \mathrm{i}\big(x^7 - 2x^5 + x^3 - 2x\big) + (x - x^3). \qquad [5]$$

The new expression $\bar{V}_{\mathcal{K}}$ is reminiscent of a quantum mechanical description of the state of a wavefunction for the "particle" $\mathcal{K}$, and will prove useful to define the orthogonality condition for the basis of the polynomial space $\mathcal{V}_n$. To proceed with this, we make use of a standard result of linear algebra (33):

Theorem (Legendre basis). *A polynomial given by*

$$P_n(x) = c_0 + c_1 x + c_2 x^2 + \ldots + c_n x^n \qquad [6]$$

can be expanded into the first $n+1$ Legendre polynomials $L_0(x), \ldots, L_n(x)$, which provide a complete basis for the knot polynomial space $\mathcal{V}_n$.

Downloaded from https://www.pnas.org by 95.75.213.112 on November 12, 2026 from IP address 95.75.213.112.

Note that the specific choice of Legendre's polynomials is purely instrumental, since any other choice of polynomials (such as Hermite's, for instance) would lead to the same results. By identifying the Jones polynomial $V_{\mathcal{K}}(x)$ with $P_n(x)$ above, we have

$$V_{\mathcal{K}}(x) \equiv P_n(x) = c_0 L_0(x) + c_1 L_1(x) + c_2 L_2(x) + \ldots + c_n L_n(x). \quad [7]$$

Therefore, each singleton of $\mathcal{V}_n$ defined by $V_{\mathcal{K}}(x)$ will be determined by the set of coordinates $\{c_i\}$, computed by

$$c_i = \int_{-1}^{1} V_{\mathcal{K}}(x) L_i(x)\, \mathrm{d}x \qquad (i = 0, \ldots, n). \quad [8]$$

To be consistent with the definition of adapted polynomials introduced by Liu and Ricca (30), a last step must involve a change of variable in Eq. **8**. Since from refs. 30 and 32 we have $x \in [1, \mathrm{e}]$, we must rescale the polynomial variable to transform the interval $[-1, 1]$ to $[1, \mathrm{e}]$, so that the appropriately rescaled Legendre polynomial denoted by $\mathcal{L}_n(x)$ satisfies the condition

$$\int_1^{\mathrm{e}} \mathcal{L}_p(x) \mathcal{L}_q(x)\, \mathrm{d}x = \delta_{pq}, \quad [9]$$

where δ_{pq} is the standard Kronecker delta. This orthogonality condition is functional to an optimal basis expansion of $V_{\mathcal{K}}(x)$ on $\mathcal{V}_n$.

Let us now apply this to the complex form of the Jones polynomial by replacing $V_{\mathcal{K}}$ with $\bar{V}_{\mathcal{K}}$ in Eq. **8**. We have

Definition 2 **(Generalized Legendre basis):** The generalized Legendre basis $\{\mathscr{L}_r(x)\}$ $(r \in \mathbb{Z})$ is given by the ordered set

$$\{\mathscr{L}_r(x)\} = \{\mathrm{i}\mathcal{L}_m(x), \ldots, \mathrm{i}\mathcal{L}_1(x), \mathcal{L}_0(x), \mathcal{L}_1(x), \ldots, \mathcal{L}_n(x)\}.$$

The condition Eq. **9** applied to the elements of the generalized Legendre basis becomes

$$\langle \mathscr{L}_p(x), \mathscr{L}_q(x) \rangle = \frac{1}{2} \int_1^{\mathrm{e}} \left(\mathscr{L}_p \mathscr{L}_q^* + \mathscr{L}_p^* \mathscr{L}_q \right) \mathrm{d}x = \delta_{pq}, \quad [10]$$

where the asterisk denotes complex conjugate. We have three cases:

(i) if $\mathscr{L}_p$ and $\mathscr{L}_q$ are both elements $\in \mathbb{R}$, we have

$$\langle \mathscr{L}_p, \mathscr{L}_q \rangle = \int_1^{\mathrm{e}} \mathcal{L}_p(x) \mathcal{L}_q(x)\, \mathrm{d}x = \delta_{pq}; \quad [11]$$

(ii) if $\mathscr{L}_p$ and $\mathscr{L}_q$ are both elements $\in \mathbb{C} \setminus \mathbb{R}$ (i.e. $\mathscr{L}_p$ and $\mathscr{L}_q$ are both elements $\in \mathrm{i}\mathbb{R}$), we have

$$\langle \mathscr{L}_p, \mathscr{L}_q \rangle = \frac{1}{2} \int_1^{\mathrm{e}} \Big[\big(\mathrm{i}\mathcal{L}_p(x)\big)\big(-\mathrm{i}\mathcal{L}_q(x)\big) + \big(-\mathrm{i}\mathcal{L}_p(x)\big)\big(\mathrm{i}\mathcal{L}_q(x)\big) \Big] \mathrm{d}x = \delta_{pq}; \quad [12]$$

(iii) if $\mathscr{L}_p \in \mathrm{i}\mathbb{R}$ and $\mathscr{L}_q \in \mathbb{R}$, we have

$$\langle \mathscr{L}_p, \mathscr{L}_q \rangle = \frac{1}{2} \int_1^{\mathrm{e}} \Big[\big(\mathrm{i}\mathcal{L}_p(x)\big)\big(\mathcal{L}_q(x)\big) + \big(-\mathrm{i}\mathcal{L}_p(x)\big)\big(\mathcal{L}_q(x)\big) \Big] \mathrm{d}x = 0. \quad [13]$$

Note the quantum mechanical interpretation of the inner product $\langle \mathscr{L}_p, \mathscr{L}_q \rangle$ as $\langle \mathscr{L}_p | \mathscr{L}_q \rangle$, where the orthogonality condition on the elements of the basis acts like an exclusion principle, $\mathscr{L}_p$ playing the role of an eigenstate of the "particle" $\mathcal{K}$.

Using Eq. **2** we can now expand the adapted knot polynomial $\bar{V}_{\mathcal{K}}(x)$ onto the generalized basis $\{\mathscr{L}_r(x)\}$ to obtain the complex expansion form $\widetilde{V}_{\mathcal{K}}(x)$. By taking advantage of the decomposition given by Eq. **3**, we have

$$\bar{V}_{\mathcal{K}}(x) \mapsto \widetilde{V}_{\mathcal{K}}(x) = \sum_{r=-m}^{n} c_{\mathcal{K},r} \mathscr{L}_r(x) = \underbrace{\mathrm{i} \sum_{j=1}^{m} c_{\mathcal{K},-j} \mathcal{L}_j(x)}_{\widetilde{V}_{\mathcal{K}}^-(x)} + \underbrace{c_{\mathcal{K},0} \mathcal{L}_0(x)}_{\widetilde{V}_{\mathcal{K}}^0(x)} + \underbrace{\sum_{i=1}^{n} c_{\mathcal{K},i} \mathcal{L}_i(x)}_{\widetilde{V}_{\mathcal{K}}^+(x)}, \quad [14]$$

where the set of coordinates $\{c_{\mathcal{K},r}\}$ of each singleton are computed by

$$c_{\mathcal{K},r} = \frac{1}{2} \int_1^{\mathrm{e}} \left[\bar{V}_{\mathcal{K}}(x) \mathscr{L}_r^*(x) + \bar{V}_{\mathcal{K}}^*(x) \mathscr{L}_r(x) \right] \mathrm{d}x \qquad (r = -m, \ldots, 0, \ldots, n). \quad [15]$$

The computation of $\{c_{\mathcal{K},r}\}$ can be done considering the three cases $r = -j < 0$, $r = 0$, and $r = i > 0$.

(i) $r = -j < 0$: the imaginary coefficients $\{c_{\mathcal{K},-j}\}$ $(j = 1, \ldots, m)$ are given by

$$\begin{aligned} c_{\mathcal{K},-j} &= \langle \bar{V}_{\mathcal{K}}^-(x), \mathrm{i}\mathcal{L}_j(x) \rangle = \frac{1}{2} \int_1^{\mathrm{e}} \left[\bar{V}_{\mathcal{K}}^{-*}(x) \big(\mathrm{i}\mathcal{L}_j(x)\big) + \big(-\mathrm{i}\mathcal{L}_j(x)\big) \bar{V}_{\mathcal{K}}^-(x) \right] \mathrm{d}x \\ &= \int_1^{\mathrm{e}} \left(a_{-m} x^m + \ldots + a_{-1} x \right) \mathcal{L}_j(x)\, \mathrm{d}x. \end{aligned} \quad [16]$$

Downloaded from https://www.pnas.org by 95.75.213.112 on November 12, 2026 from IP address 95.75.213.112.

(ii) $r = i > 0$: the real coefficients $\{c_{\mathcal{K},i}\}$ $(i = 1, \ldots, n)$ are given by

$$c_{\mathcal{K},i} = \langle \bar{V}^{+}_{\mathcal{K}}(x), \mathcal{L}_i(x) \rangle = \int_1^{\mathrm{e}} \bar{V}^{+}_{\mathcal{K}}(x) \mathcal{L}_i(x)\, \mathrm{d}x = \int_1^{\mathrm{e}} \left(a_1 x + \ldots + a_n x^n\right) \mathcal{L}_i(x)\, \mathrm{d}x. \quad [17]$$

(iii) $r = 0$: the "zero" coefficient $c_{\mathcal{K},0}$ is given by $c_{\mathcal{K},0} = c^{-}_{\mathcal{K},0} + c^{0}_{\mathcal{K},0} + c^{+}_{\mathcal{K},0}$, where

$$\begin{aligned} c^{-}_{\mathcal{K},0} &= \langle \bar{V}^{-}_{\mathcal{K}}(x), \mathrm{i}\mathcal{L}_0(x) \rangle = \frac{1}{2} \int_1^{\mathrm{e}} \left[\bar{V}^{-*}_{\mathcal{K}}(x) \left(\mathrm{i}\mathcal{L}_0(x)\right) + \left(-\mathrm{i}\mathcal{L}_0(x)\right) \bar{V}^{-}_{\mathcal{K}}(x) \right] \mathrm{d}x \\ &= \int_1^{\mathrm{e}} \left(a_{-m} x^m + \ldots + a_{-1} x\right) \mathcal{L}_0(x)\, \mathrm{d}x, \end{aligned} \quad [18]$$

$$c^{0}_{\mathcal{K},0} = \langle a_0, \mathcal{L}_0(x) \rangle = \int_1^{\mathrm{e}} a_0 \mathcal{L}_0(x)\, \mathrm{d}x, \quad [19]$$

$$c^{+}_{\mathcal{K},0} = \langle \bar{V}^{+}_{\mathcal{K}}(x), \mathcal{L}_0(x) \rangle = \int_1^{\mathrm{e}} \bar{V}^{+}_{\mathcal{K}}(x) \mathcal{L}_0(x)\, \mathrm{d}x = \int_1^{\mathrm{e}} \left(a_1 x + \ldots + a_n x^n\right) \mathcal{L}_0(x)\, \mathrm{d}x. \quad [20]$$

Summing up the three terms above we have

$$c_{\mathcal{K},0} = \int_1^{\mathrm{e}} \left(a_{-m} x^m + \ldots + a_{-1} x + a_0 + a_1 x + \ldots + a_n x^n\right) \mathcal{L}_0(x)\, \mathrm{d}x. \quad [21]$$

The inner product of the Jones polynomials of the knots $\mathcal{K}$ and $\mathcal{K}'$ becomes then

$$\langle \widetilde{V}_{\mathcal{K}}, \widetilde{V}_{\mathcal{K}'} \rangle = \frac{1}{2} \int_1^{\mathrm{e}} \left[\widetilde{V}^{*}_{\mathcal{K}}(x)\, \widetilde{V}_{\mathcal{K}'}(x) + \widetilde{V}^{*}_{\mathcal{K}'}(x)\, \widetilde{V}_{\mathcal{K}}(x) \right] \mathrm{d}x. \quad [22]$$

Assuming $m < m'$ and $n < n'$, we have $c_{\mathcal{K},-j} c_{\mathcal{K}',j} = 0\ \forall j = m+1, \ldots, m'$ (no summation over j), and $c_{\mathcal{K},i} c_{\mathcal{K}',i} = 0\ \forall i = n+1, \ldots, n'$ (no summation over i), so that from Eq. **22** we finally have

$$\langle \widetilde{V}_{\mathcal{K}}, \widetilde{V}_{\mathcal{K}'} \rangle = \sum_{j=1}^{m} c_{\mathcal{K},-j} c_{\mathcal{K}',j} + c_{\mathcal{K},0} c_{\mathcal{K}',0} + \sum_{i=1}^{n} c_{\mathcal{K},i} c_{\mathcal{K}',i}. \quad [23]$$

The derivation of this set of coordinates for each singleton of $\mathcal{V}_n$ represents an important result for the computation of the decaying paths on the knot polynomial space.

Probability of Occurrence of a Topological State. In order to compute the probability of occurrence of a given knot type $\mathcal{K}$ we must first determine the probability density $\rho(\mathcal{K})$; this is given by

$$\rho(\mathcal{K}) = \langle \widetilde{V}_{\mathcal{K}}, \widetilde{V}_{\mathcal{K}} \rangle = \int_1^{\mathrm{e}} \widetilde{V}^{*}_{\mathcal{K}}(x) \widetilde{V}_{\mathcal{K}}(x)\, \mathrm{d}x = \sum_{r=-m}^{n} c^2_{\mathcal{K},r}. \quad [24]$$

The *probability of occurrence* $p_r(\mathcal{K})$ of each r-(eigen)state of $\mathcal{K}$ is thus given by

$$p_r(\mathcal{K}) = \frac{c^2_{\mathcal{K},r}}{\sum_r c^2_{\mathcal{K},r}} \qquad r = -m, \ldots, n, \quad [25]$$

where $c^2_{\mathcal{K},r}$ represents the density distribution of each state, and $\sum_r p_r(\mathcal{K}) = 1$. We have

Definition 3 **(Entanglement index):** Given the probability of occurrence $p_r(\mathcal{K})$, the entanglement index associated with the appearance of each topological state $\mathcal{K}$ is defined by

$$\varepsilon(\mathcal{K}) = -\sum_{r=-m}^{n} p_r(\mathcal{K}) \ln p_r(\mathcal{K}). \quad [26]$$

This index, computed for each vortex knot, provides a measure of the topological complexity of that state. Since $\varepsilon(\mathcal{K})$ measures the decreasing amount of structural information stored in a given topological state, it is tempting to regard this quantity as a negative entropy (or "negentropy") (34), interpreting (with a negative sign) two different types of entropy: the standard entropy of information theory (à la Shannon), based purely on the mathematical information provided by the algebraic expression of the knot polynomial, and the thermodynamic entropy of fluid mechanics, associated with the physical energy and organization of the fluid system.

Results

We compute the entanglement index $\varepsilon(\mathcal{K})$ of knots, links, and composites (connected sums) up to $c_{\min} = 8$, including mirror images and noninvertible ones. For each $\mathcal{K}$ we consider the standard Jones polynomial rewritten in complex expansion form $\widetilde{V}_{\mathcal{K}}(x)$, compute the singleton coordinates $\{c_{\mathcal{K},r}\}$, the probability $p_r(\mathcal{K})$, and the associated index $\varepsilon(\mathcal{K})$. Since the unknot has Jones polynomial $V_{\boldsymbol{U}} = 1$, using Eq. **26** we take $\varepsilon = 0$ to identify this state. All data are collected and presented in the KnotData tables of the *SI Appendix*.

Downloaded from https://www.pnas.org by 95.75.213.112 on November 12, 2026 from IP address 95.75.213.112.

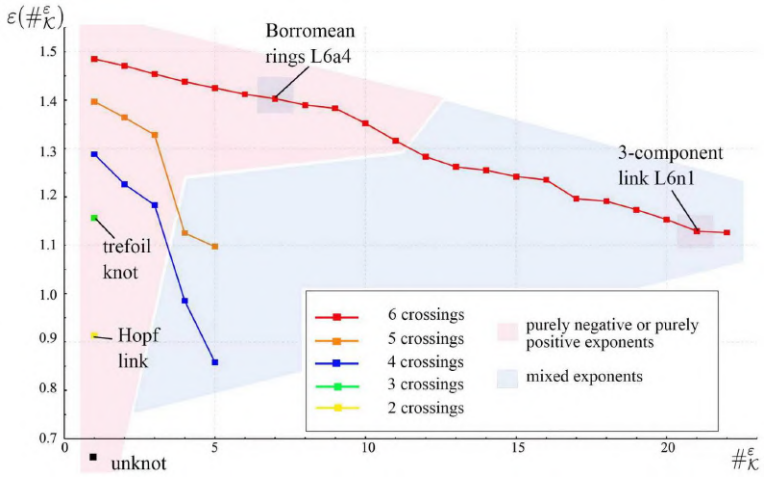

Fig. 3. ε-values (denoted by square dots) plotted against the knot type number $\#^{\varepsilon}_{\mathcal{K}}$ for knots, links, and composites up to 6 crossings. The set $\{\#^{\varepsilon}_{\mathcal{K}}\}$ is ordered according to the decreasing value of ε; square dots are connected by segments to highlight the general trend. Crossing families are denoted by different colors as indicated in *Inset*. The pink region denotes knot types whose polynomials have the same exponent sign (all purely negative or all purely positive); the light blue region denotes knot types whose polynomials have mixed exponent signs. The Borromean rings denoted by L6a4 and the 3-component link L6n1 (identified by opposite background color) represent two exceptions.

Knots, Links, and Composites up to 6 Crossings. Let us first consider knots, links, and composites up to 6 crossings: by examining all variants, including mirror counterparts and with reversed orientation, we have 15 topological types with up to $c_{\min} = 4$, 12 with $c_{\min} = 5$, 61 with $c_{\min} = 6$. The entanglement index is computed for each knot type $\mathcal{K}$, and data are plotted according to the decreasing value of ε. The sequence of knot types on the horizontal axis (denoted by the label $\#^{\varepsilon}_{\mathcal{K}}$) is ordered according to decreasing values of ε. Computed values shown in Fig. 3 are denoted by squared dots, and are connected by segments to highlight the general trend: red denotes 6-crossing knot types, orange 5-crossing, blue 4-crossing, green 3-crossing (i.e. the trefoil knot), yellow 2-crossing (i.e. the Hopf link), and black the unknot. As we see for increasing values of $c_{\min}$ each ε-distribution remains well-separated and ordered one on top of the other for increasing $c_{\min}$-values. This marked separation is in good agreement with what is observed in experiments, where complex knots are seen to reduce consistently their topological complexity in time. Note that this feature appears to be generic and independent of the crossing number.

A second, more subtle feature emerges from the algebraic representation of the Jones polynomial. According to the transformations $V_{\mathcal{K}}(x) \mapsto \bar{V}_{\mathcal{K}}(x) \mapsto \tilde{V}_{\mathcal{K}}(x)$, terms containing only purely negative or purely positive exponents, and terms containing mixed exponent signs get separated into two distinct groups given by a real and imaginary part (remember that the exponents of a mirror image of a given knot have opposite signs). Remarkably, this decomposition is (almost) perfectly reflected in the net separation of the distributions of the ε-values into two distinct regions of the plot denoted by different background colors: the pink region denotes knot polynomials whose exponents have all purely negative or purely positive signs; the light blue region denotes polynomials whose exponents have mixed signs. Two exceptions, marked by the opposite background color, are present: one is the Borromean rings denoted by L6a4, the other is the 3-component link L6n1. These two misplaced knots represent a modest 6% of all the knot types considered.

Comparison with Previous Results. For completeness let us compare these results with what has been done earlier. Let us start with a comparison with the results obtained in terms of complexity degree $\chi = \chi(\mathcal{K})$ (3). This is defined by

$$\chi(\mathcal{K}) = \ln[1 + \mathrm{d}(V_{\mathcal{K}}, V_{\boldsymbol{U}})], \qquad [27]$$

where $\mathrm{d}(V_{\mathcal{K}}, V_{\boldsymbol{U}})$ denotes the geodesic distance between the adapted knot polynomial of $\mathcal{K}$ and the unknot $\boldsymbol{U}$. Fig. 4 shows the plot $\chi = \chi(\#^{\chi}_{\mathcal{K}})$ for the same set of knots, now ordered according to the decreasing values of χ given by the sequence $\{\#^{\chi}_{\mathcal{K}}\}$. The two dominant features discussed for the $\varepsilon(\#^{\varepsilon}_{\mathcal{K}})$-plot are reproduced in the $\chi(\#^{\chi}_{\mathcal{K}})$-plot: same behavior for the distributions of the crossing-family values, and same net separation between the pink and the light blue region. In this case only the 3-component link L6n1 appears misplaced. As we can see both data presentations show overall analytical consistency.

We now compare the ε-data with the specific results obtained by earlier works. Three sets of data are available: one provided by the group of Vazquez et al. (35), one by the group of Irvine et al. (13), and one by the group of Liu et al. (18). The 17 unlinking paths from the torus link $T(2,6)$ represented by the sequence of the torus family and the knots $3_1\#3_1$, A, B, C, D (35), and denoted by the set of colored arrowed lines shown on the right-hand side of the plots of Figs. 4 and 5, are well captured by the χ-plot, and even better by the ε-plot, where the cascade is perfectly reproduced by the probability occurrence represented by the position of the ε-data points in the pink area. The same can be said for the cascade of the 6_2 studied by Irvine et al. (13) given by the sequence 6_2, L4a1, $T(2,3)$, $T(2,2)$ and the unknot, and denoted by the magenta dot-dash arrowed lines shown in Fig. 5, where the ε unlinking paths computed are in perfect agreement with what has been observed in simulations.

Finally we consider the cascade of superfluid Borromean rings observed by Liu et al. (18). The cascade has been analyzed considering 17 different initial conditions. Since different initial conditions generate different unlinking pathways (as shown in the diagram of

Downloaded from https://www.pnas.org by 95.75.213.112 on November 12, 2026 from IP address 95.75.213.112.

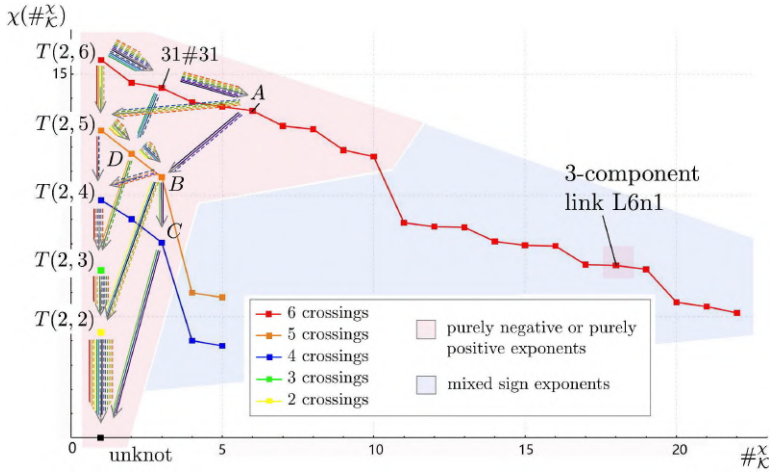

Fig. 4. Complexity degree χ (values denoted by square dots) plotted against the knot type number $\#^{\chi}_{\mathcal{K}}$ for knots, links, and composites up to 6 crossings. The set $\{\#^{\chi}_{\mathcal{K}}\}$ is ordered according to the decreasing value of χ; square dots are connected by segments to highlight the general trend. Crossing families are denoted by different colors as indicated in *Inset*. The pink region denotes knot types whose polynomials have the same exponent sign (all purely negative or all purely positive); the light blue region denotes knot types whose polynomials have mixed exponent signs. The 3-component link L6n1 (identified by the opposite background color) represents an exception. The colored lines denoted by arrows represent the pathways followed by the cascade of the torus link $T(2,6)$ analyzed in refs. 1–3 and 35 (labels as in the original notation).

Fig. 2, *Right*), the decaying probability associated with each topological state takes this into account. Here for simplicity we represent a synthesis of all possible transitions, independent from their relative occurrence induced by their specific initial conditions. In this case the computed ε-values do not represent a specific decaying path, but they give an indication of the dominant phenomenon. The observed cascade toward the formation of a Whitehead link and a trefoil knot, and the subsequent formation of the other states, is also well captured by the decreasing values of $\varepsilon(\mathcal{K})$ as shown by the double dot-dash arrowed lines.

Knots, Links, and Composites up to 8 Crossings. The results obtained so far confirm the validity of the approach based on the ε-analysis, so we extend this study to knots, links, and composites up to 8 crossings, 108 with $c_{\min} = 7$, and 455 with $c_{\min} = 8$. This involves the examination of further 563 variants, that after the elimination of duplicates reduces the total number to 198 knot types. Data are shown in Fig. 6, where ε-values are plotted for all the knot families considered so far, including the 7-crossing family (in purple), and the 8-crossing family (in coral).

In accordance with previous results, all the distributions appear to be well separated one on top of the other for increasing $c_{\min}$, and throughout the whole spectrum of the knot types examined. The discriminatory ability of the ε-measure to detect different knot families is confirmed. By examining the algebraic structure of the knot polynomials we confirm also the net separation between the pink and the light blue regions that distinguish polynomials, whose powers are given by only purely negative or positive exponent signs (pink), from those with mixed signs (light blue). Only a few knot types (denoted by opposite background color) result "misplaced,"

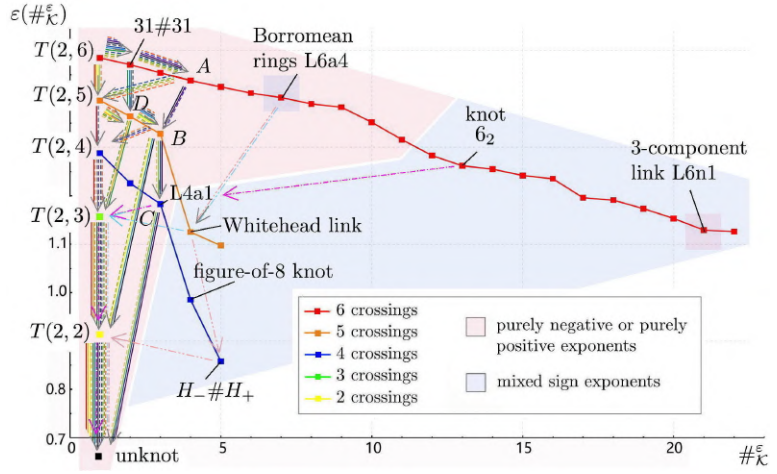

Fig. 5. Entanglement index ε plotted against $\#^{\varepsilon}_{\mathcal{K}}$ for knots, links, composites up to 6 crossings. The set $\{\#^{\varepsilon}_{\mathcal{K}}\}$ is ordered according to the decreasing value of ε; square dots are connected by segments to highlight the general trend. Crossing families are denoted by different colors as indicated in *Inset*. The pink region denotes knot types whose polynomials have the same exponent sign (all purely negative or all purely positive); the light blue region denotes knot types whose polynomials have mixed exponent signs. Dotted-dashed lines with big arrows denote the observed topological cascade of the 6_2 knot and the Borromean rings analyzed in refs. 13 and 18, respectively.

Downloaded from https://www.pnas.org by 95.75.213.112 on November 12, 2026 from IP address 95.75.213.112.

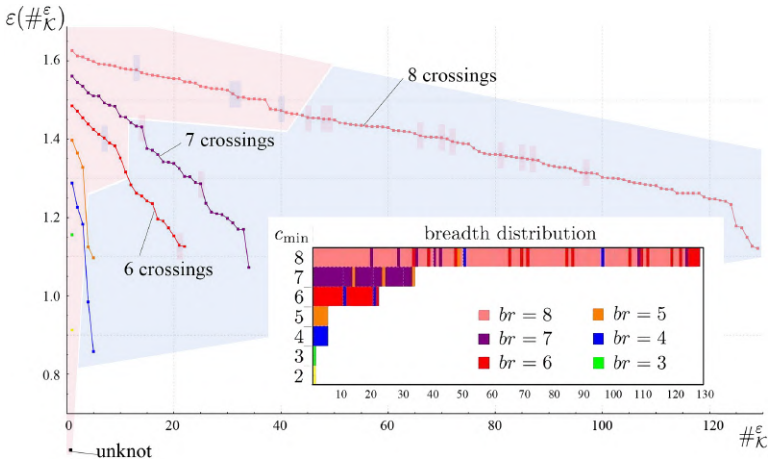

Fig. 6. Entanglement index ε plotted against $\#^{\varepsilon}_{\mathcal{K}}$ for knots, links, composites up to 8 crossings. The set $\{\#^{\varepsilon}_{\mathcal{K}}\}$ is ordered according to the decreasing value of ε; square dots are connected by segments to highlight the general trend. The distribution of the 8-crossing values remains well separated from the 7-crossing values and on top of all the others, in accordance with increasing values of $c_{\min}$. The net separation between the pink and the light blue regions is evident. The distribution of breadth values for each crossing family is shown in *Inset*.

with a relative distribution that varies between 9% (for $c_{\min} = 6$) and 11% (for $c_{\min} = 8$). A table with information on the misplaced knot types is shown in *SI Appendix*, Fig. S1.

Another interesting aspect comes from the computation of the *breadth* (or span) $\mathrm{br}(V_{\mathcal{K}})$ of the polynomial (36). This is defined by

$$\mathrm{br}(V_{\mathcal{K}}) = \max(\deg V_{\mathcal{K}}) - \min(\deg V_{\mathcal{K}}), \qquad [28]$$

where $\max/\min(\deg V_{\mathcal{K}})$ denotes the maximum/minimum degree of the Jones polynomial; $\mathrm{br}(V_{\mathcal{K}})$ quantifies the "spread" (or variability) of the coefficients of $V_{\mathcal{K}}$. The distribution of breadth values is shown in *Inset* of Fig. 6. Remarkably, we find that the majority of knot types examined satisfy the equality $\mathrm{br}(V_{\mathcal{K}}) = c_{\min}$, with only 1% to 2% of all knot types obeying the Morton–Franks–Williams inequality $\mathrm{br}(V_{\mathcal{K}}) > c_{\min}$.

Discussion

The reformulation of the Jones polynomial in a complex form, where the real part of the algebraic expression collects all positive powers and the imaginary part takes care of all the negative powers, represents a major advancement for the computation of the properties associated with the topological state of a vortex tangle, and for measuring its topological complexity in terms of an entanglement index. The dynamical decaying process is identified by interpreting the evolutionary paths followed by the physical system as geodesic flows determined by the topological cascade of vortex knots in an abstract knot polynomial space. To determine the properties of this space we make use of the adapted version of the Jones polynomial (3, 32), where we identify fluid knots as singletons of this space. According to the metric given by expanding the knot polynomial into a generalized Legendre basis, we determine the coordinates of each singleton, compute the probability density of occurrence of each knot $\mathcal{K}$, and determine the corresponding entanglement index $\varepsilon(\mathcal{K})$. The computation of this index is carried out considering knots up to 8 crossings, including 198 distinct topological states given by single or composite knots, and 651 variants given by their different prescriptions of orientation and chirality. Computed data are compared with the actual decaying paths observed in experiments (13, 18, 35), and we find a very good agreement between theoretical predictions and experimental results. Since another measure of topological complexity, called complexity degree χ, was introduced in literature (3), a comparative analysis between ε-values and χ-values has been carried out confirming that the ε-based analysis provides a more reliable tool for this type of study. Details of this comparison are presented in *SI Appendix*, Fig. S2.

The present results demonstrate that $\varepsilon(\mathcal{K})$ proves to be a robust identifier of the topological cascade of fluid knots and links, irrespective of the specific topological complexity. This measure proves to be also a strong discriminator between knots whose polynomials have the same exponent sign from those with mixed signs. This feature associated with the analysis of the breadth of the corresponding knot polynomial provides useful information for the statistical study of geometric aspects (symmetry and chirality) related to kinetic energy and helicity of vortical flows.

Since in recent years work on knotted configurations and defects in soft and biological matter has greatly intensified (7), questions related to composite knots and chirality emerged as important issues for possible applications in science and technology (37). To show how the present analysis helps to address these other aspects we conclude with a comparative computation of the topological complexity of the knot 7_1, its mirror image 7_1^*, their connected sums $7_1 \# 7_1$ and $7_1 \# 7_1^*$, and their disjoint unions $7_1 \sqcup 7_1$ and $7_1 \sqcup 7_1^*$, considering the corresponding χ- and ε-values. The Jones polynomial of the connected sum and the disjoint union of the knots $\mathcal{K}$ and $\mathcal{K}'$ is given by the standard formulas (38)

$$V_{\mathcal{K}\#\mathcal{K}'} = V_{\mathcal{K}}\, V_{\mathcal{K}'}\,, \quad V_{\mathcal{K}\sqcup\mathcal{K}'} = \delta\, V_{\mathcal{K}}\, V_{\mathcal{K}'}, \qquad [29]$$

where, from the definition of $\delta = -q^{1/2} - q^{-1/2} = -x - x^{-1}$, we take $\delta = 1.9814$ for the χ values, and $\delta = 0.1193$ for the ε values. The computed values of χ and ε are shown in Fig. 7 listed by increasing order of magnitude. Both measures quantify the complexity

Downloaded from https://www.pnas.org by 95.75.213.112 on November 12, 2026 from IP address 95.75.213.112.

Knot type	Jones polynomial	Complexity degree (χ)	Entanglement index (ε)	KnotPlot image
$7_1 \# 7_1^*$ opposite chirality	$7 - \frac{1}{q^7} + \frac{1}{q^6} - \frac{2}{q^5} + \frac{3}{q^4} - \frac{4}{q^3} + \frac{5}{q^2} - \frac{5}{q}$ $-5q + 5q^2 - 4q^3 + 3q^4 - 2q^5 + q^6 - q^7$	13.1374	1.8412	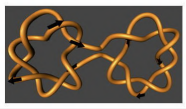
$7_1 \sqcup 7_1^*$ opposite chirality	$\frac{1}{q^{15/2}} + \frac{1}{q^{11/2}} - \frac{1}{q^{9/2}} + \frac{1}{q^{7/2}} - \frac{1}{q^{5/2}} - \frac{2}{\sqrt{q}}$ $-2\sqrt{q} - q^{5/2} + q^{7/2} - q^{9/2} + q^{11/2} + q^{15/2}$	14.2358	1.8765	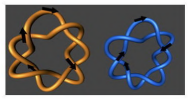
7_1	$-\frac{1}{q^{10}} + \frac{1}{q^9} - \frac{1}{q^8} + \frac{1}{q^7} - \frac{1}{q^6} + \frac{1}{q^5} + \frac{1}{q^3}$	18.510	1.5603	
7_1^*	$-q^{10} + q^9 - q^8 + q^7 - q^6 + q^5 + q^3$			
$7_1 \# 7_1$ same chirality	$\frac{1}{q^{20}} - \frac{2}{q^{19}} + \frac{3}{q^{18}} - \frac{4}{q^{17}} + \frac{5}{q^{16}} - \frac{6}{q^{15}} + \frac{5}{q^{14}}$ $-\frac{6}{q^{13}} + \frac{5}{q^{12}} - \frac{4}{q^{11}} + \frac{3}{q^{10}} - \frac{2}{q^9} + \frac{2}{q^8} + \frac{1}{q^6}$	38.0429	1.8908	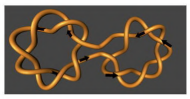
$7_1 \sqcup 7_1$ same chirality	$-\frac{1}{q^{41/2}} + \frac{1}{q^{39/2}} - \frac{1}{q^{37/2}} + \frac{1}{q^{35/2}} - \frac{1}{q^{33/2}}$ $+\frac{1}{q^{31/2}} + \frac{1}{q^{29/2}} + \frac{1}{q^{27/2}} + \frac{1}{q^{25/2}} - \frac{1}{q^{23/2}}$ $+\frac{1}{q^{21/2}} - \frac{1}{q^{19/2}} - \frac{2}{q^{15/2}} - \frac{1}{q^{13/2}} - \frac{1}{q^{11/2}}$	39.1607	1.8997	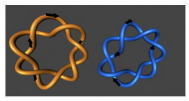

Fig. 7. Complexity degree χ and entanglement index ε values for the knot 7_1, its mirror image 7_1^*, their connected sums $7_1 \# 7_1$, $7_1 \# 7_1^*$, and their disjoint unions $7_1 \sqcup 7_1$, $7_1 \sqcup 7_1^*$. The χ and ε values are listed in increasing order of magnitude with their corresponding images obtained by KnotPlot (39).

of the connected sum by a value lower than that of the disjoint union. More subtle aspects are related to the effects of orientation and chirality, but these require an ad hoc discussion that is beyond the scope of this work.

Conclusions

The interpretation of decaying paths in terms of geodesic flows on a knot polynomial space, the methods used to determine its basis, and the extent to which this analysis has been carried out represent further progress for the study of complex systems. The techniques introduced can be readily extended to an even wider class of knots and links, and other types of knot polynomials such as the Alexander polynomial. This further extension can be certainly achieved by the implementation of machine learning techniques and automatic computation. The use of other types of knot polynomials, such as HOMFLYPT (31) in 2 or more variables, will require more elaborate analytical tools for the construction of the metric space, and work in this direction is also in progress. Since the present approach shows great capability to identify the preferential routes that govern the dynamical decay of fluid systems, the same method shows potentials for application in other contexts, such as polymer physics, where a great deal of topological complexity is present and huge datasets are available. Moreover, we believe this type of work will also help to address the fundamental question that regards the relation between topological reorganization and energy transfers across scales.

Data, Materials, and Software Availability. All study data are included in the article and are taken from the KnotData tables included in the *SI Appendix* and are publicly available.

ACKNOWLEDGMENTS. Financial support from the Beijing Natural Science Foundation (Grant nos. IS23030 and Z180007) and the Natural Science Foundation of China (Grant no. 11572005) is kindly acknowledged. Y.Z. wishes to acknowledge also financial support from the Natural Science Foundation of China (Grant no. 12234019). R.L.R. acknowledges the kind hospitality of Beijing University of Technology, where part of this work was done.

1. K. Shimokawa, K. Ishihara, I. Grainge, D. J. Sherratt, M. Vazquez, Ftsk-dependent XerCD-dif recombination unlinks replication catenanes in a stepwise manner. *Proc. Natl. Acad. Sci. U.S.A.* **110**, 20906–20911 (2013).
2. X. Liu, R. L. Ricca, Knots cascade detected by a monotonically decreasing sequence of values. *Sci. Rep.* **6**, 24118 (2016).
3. X. Liu, R. L. Ricca, X. F. Li, Minimal unlinking pathways as geodesics in knot polynomial space. *Commun. Phys.* **3**, 136 (2020).
4. A. Martinez *et al*., Mutually tangled colloidal knots and induced defect loops in nematic fields. *Nat. Mater.* **13**, 258–263 (2014).
5. J. Hao, Y. Yang, Magnetic knot cascade via the stepwise reconnection of helical flux tubes. *J. Fluid Mech.* **912**, A48 (2021).
6. RL Ricca, X Liu, Eds., *Knotted Fields, Lecture Notes in Mathematics* (Springer-Nature, Switzerland, 2024), vol. 2344.
7. L. Tubiana *et al*., Topology in soft and biological matter. *Phys. Rep.* **1075**, 1–137 (2024).
8. R. L. Ricca, "Topological fluid dynamics and knotted fields" in *Encyclopedia of Mathematical Physics*, R. Szabo, M. Bojowald, Eds. (Academic Press, ed. 2, 2025), vol. 4, pp. 245–255.
9. A. Villois, D. Proment, G. Krstulovich, Evolution of a superfluid vortex filament tangle driven by the Gross-Pitaevskii equation. *Phys. Rev. E* **93**, 061103(R) (2016).

Downloaded from https://www.pnas.org by 95.75.213.112 on November 12, 2026 from IP address 95.75.213.112.

10. T. Nakagawa, S. Inui, M. Tsubota, Internal structure of localised quantised vortex tangles. *Phys. Rev. B* **104**, 094510 (2021).
11. J. I. Polanco, N. P. Müller, G. Krstulovic, Vortex clustering, polarisation and circulation intermittency in classical and quantum turbulence. *Nat. Commun.* **12**, 7090 (2021).
12. D. Kleckner, W. T. M. Irvine, Creation and dynamics of knotted vortices. *Nat. Phys.* **9**, 253–258 (2013).
13. D. Kleckner, L. H. Kauffman, W. T. M. Irvine, How superfluid vortex knots untie. *Nat. Phys.* **12**, 650–655 (2016).
14. S. Zuccher, R. L. Ricca, Relaxation of twist helicity in the cascade process of linked quantum vortices. *Phys. Rev. E* **95**, 053109 (2017).
15. W. K. Bai, T. Yang, W. M. Liu, Topological transition from superfluid vortex rings to isolated knots and links. *Phys. Rev. A* **102**, 063318 (2020).
16. S. Zuccher, R. L. Ricca, Creation of quantum knots and links driven by minimal surfaces. *J. Fluid Mech.* **942**, A8 (2022).
17. X. Liu, R. L. Ricca, H. Guan, "A topological approach to vortex knots and links" in *Knotted Fields, Lecture Notes in Mathematics*, R. L. Ricca, X. Liu, Eds. (Springer-Nature, Switzerland, 2024), vol. 2344, pp. 1–36.
18. H. Guan, S. Zuccher, X. Liu, Topological cascade of quantum Borromean rings. *Phys. Fluids* **37**, 024126 (2025).
19. W. Shen, J. Yao, Y. Yang, Designing turbulence with entangled vortices. *Proc. Natl. Acad. Sci. U.S.A.* **121**, e2405351121 (2024).
20. B. Hnat, S. Chapman, N. Watkins, Topology of turbulence within collisionless plasma reconnection. *Sci. Rep.* **13**, 18665 (2023).
21. H. Kedia, I. Bialynicki-Birula, D. Peralta-Salas, W. T. M. Irvine, Tying knots in light fields. *Phys. Rev. Lett.* **111**, 150404 (2013).
22. I. I. Smalyukh, Review: Knots and other new topological effects in liquid crystals and colloids. *Rep. Prog. Phys.* **83**, 106601 (2020).
23. T. Annala, R. Zamora-Zamora, M. Möttönen, Topologically protected vortex knots and links. *Commun. Phys.* **5**, 309 (2022).
24. R. G. Cooper, M. Mesgarnezhad, A. W. Baggaley, C. F. Barenghi, Knot spectrum of turbulence. *Sci. Rep.* **9**, 10545 (2019).
25. C. F. Barenghi, "Tangled vortex lines: Dynamics, geometry and topology of quantum turbulence" in *Knotted Fields, Lecture Notes in Mathematics*, R. L. Ricca, X. Liu, Eds. (Springer-Nature, Switzerland, 2024), vol. 2344, pp. 243–279.
26. C. C. Adams, *The Knot Book* (American Mathematical Society, 2004).
27. J. B. Kruskal, On the shortest spanning subtree of a graph and the traveling salesman problem. *Proc. Am. Math. Soc.* **7**, 48–50 (1956).
28. E. W. Dijkstra, A note on two problems in connexion with graphs. *Numer. Math.* **1**, 269–271 (1959).
29. M. A. Nielsen, M. R. Dowling, M. Gu, A. C. Doherty, Quantum computation as geometry. *Science* **31**, 1133–1135 (2006).
30. X. Liu, R. L. Ricca, The Jones polynomial for fluid knots from helicity. *J. Phys. A Math. Theor.* **45**, 205501 (2012).
31. X. Liu, R. L. Ricca, On the derivation of the HOMFLYPT polynomial invariant for fluid knots. *J. Fluid Mech.* **773**, 34–48 (2015).
32. R. L. Ricca, X. Liu, A new framework for the Jones polynomial of fluid knots. *J. Knot Theory Ramif.* **35**, 2340024 (2026).
33. S. Leon, *Linear Algebra with Applications* (Pearson Education Inc., London, 2010).
34. L. Brillouin, The negentropy principle of information. *J. Appl. Phys.* **24**, 1152 (1953).
35. R. Stolz *et al*., Pathways of DNA unlinking: A story of stepwise simplification. *Sci. Rep.* **7**, 12420 (2017).
36. W. B. R. Lickorish, *An Introduction to Knot Theory, Graduate Texts in Mathematics* (Springer, 1997), vol. 175.
37. D. Hall, J. S. B. Tai, L. H. Kauffman, I. I. Smalyukh, Fusion and fission of particle-like chiral nematic vortex knots. *Nat. Phys.* **22**, 103–111 (2026).
38. W. B. R. Lickorish, K. C. Millett, The new polynomial invariants of knots and links. *Math. Mag.* **61**, 3–23 (1988).
39. R. G. Scharein, The knotplot site. https://knotplot.com. Accessed 18 October 2026.

Downloaded from https://www.pnas.org by 95.75.213.112 on November 12, 2026 from IP address 95.75.213.112.